Localization effects induced by decoherence in superpositions of many-spin quantum states

Gonzalo A. Álvarez[*] and Dieter Suter[†]

Fakultät Physik, Technische Universität Dortmund, Dortmund, Germany

The spurious interaction of quantum systems with their environment known as decoherence leads, as a function of time, to a decay of coherence of superposition states. Since the interactions between system and environment are local, they can also cause a loss of spatial coherence: correlations between spatially distant parts of the system are lost and the equilibrium states can become localized. This effect limits the distance over which quantum information can be transmitted, e.g., along a spin chain. We investigate this issue in a nuclear magnetic resonance quantum simulator, where it is possible to monitor the spreading of quantum information in a three-dimensional network: states that are initially localized on individual spins (qubits) spread under the influence of a suitable Hamiltonian apparently without limits. If we add a perturbation to this Hamiltonian, the spreading stops and the system reaches a limiting size, which becomes smaller as the strength of the perturbation increases. This limiting size appears to represent a dynamical equilibrium. We present a phenomenological model to describe these results.

I. INTRODUCTION

Controlling quantum-mechanical systems has received increasing attention in recent years [1], mainly because we are starting to be able to perform computations with quantum-mechanical systems. This has the potential of solving computational problems for which no efficient algorithm exists for classical computers [2–4]. However, we will only be able to realize this potential if we learn to control large quantum systems with high reliability. The control of *small* quantum systems has been thoroughly explored in the last years [1]; however, the study and control of *large* quantum systems has not been tackled so far. The reason for this is partly the difficulty of simulating large quantum systems on classical computers, which limits the number of qubits to about 20 when the system is in a pure state [5,6]. Additionally, it is also possible to calculate the dynamics of mixed states if the initial state is localized by using quantum parallelism of a single pure state evolution [7,8]. On the other hand, the present primitive state of quantum computation only allows incomplete control of large quantum states. So far, the only physical system that offers this possibility is nuclear magnetic resonance (NMR) of dipolar coupled spins [9–11]. In particular, the main problems are the lack of individual addressing of qubits and decoherence. The latter degrades the quantum information of a given state [12]. Decoherence was shown to increase as the size of the quantum system increases, making the largest systems the most sensitive to perturbations [9–11,13–15]. While reducing the perturbation strength typically reduces decoherence, the decoherence time in complex and large systems can be independent of the perturbation strength over a range of coupling strengths [16,17].

Decoherence is well known as a process that causes the decay of quantum information. Avoiding or reducing decoherence is thus the main ingredient for implementing large-scale quantum computers. Several techniques have been proposed for this purpose, including dynamical decoupling [18], decoherence-free subspaces [19], and quantum error correction [20,21]. These proposals have been tested on small systems of nuclear spins [22], trapped ions [23], and spin model quantum memories [24,25]. Some of these techniques were successfully applied to large quantum systems with thousands of qubits where their decoherence time was extended by almost two orders of magnitude [10,15].

Decoherence not only affects the survival time of quantum information, it also affects the distance over which it can be transmitted [26–34]. For example, spin systems, and in particular spin chains, can be used to transfer quantum information over large distances [35,36]. This kind of system was studied with liquid-state NMR for small numbers of spins [37–41] and with solid-state NMR for slightly larger numbers [42–44]. However, once decoherence is considered, it was shown in the simplest two-spin quantum channel that when the effective system-environment interaction exceeds a given strength, it becomes impossible to perform even a simple SWAP operation [33,45]. Instead of having the expected oscillatory transfer of a state going back and forth between the two spins, an overdamped dynamics due to the appearance of a localized state appears at a critical value or exceptional point of the perturbation strength [45–49]. Similarly, this could be observed in a three-spin chain. If one spin is suffering a perturbation, when it exceeds a given strength the dynamics localizes in the remaining two spins [50]. In a more general situation with longer spin chains, it was recently pointed out that imperfections or disorder of the spin coupling that drives the state transfer can induce localization of the quantum information [26–31,34] in a process related to Anderson localization [51,52]. In more complex three-dimensional (3D) spin-network topologies, we demonstrated experimentally a similar behavior by studying the localization effects induced by the finite precision of quantum gate operations used for transferring quantum states [32].

In this paper, we extend our previous work [32], where we prepared the system first as individual, uncorrelated spins and measured the buildup of clusters of correlated spins of increasing size. Introducing a perturbation to the Hamiltonian

---

[*]galvarez@e3.physik.uni-dortmund.de
[†]Dieter.Suter@tu-dortmund.de

that generates these clusters, we find that the size of the cluster reaches an upper bound. This upper bound appears to be a dynamic equilibrium: if the cluster size is initially larger than this equilibrium value, it decreases under the effect of the perturbed Hamiltonian, while the unperturbed Hamiltonian leads to an increase. The equilibrium size decreases with increasing strength of the perturbation. For these experiments, we use a solid-state NMR quantum simulator. While this system does not allow addressing of individual qubits, it represents an excellent test bed for studying different aspects of decoherence and information transfer.

II. THE QUANTUM SIMULATOR

We consider a system of equivalent spins $I = 1/2$ in the presence of a strong magnetic field. The Hamiltonian of the system is

$$
\begin{aligned}
\widehat{\mathcal{H}} &= \widehat{\mathcal{H}}_z + \widehat{\mathcal{H}}_{dd} \\
&= \omega_z \sum_i \hat{I}_z^i + \sum_{i<j} d_{ij} \left[2\hat{I}_z^i \hat{I}_z^j - \left(\hat{I}_x^i \hat{I}_x^j + \hat{I}_y^i \hat{I}_y^j \right) \right],
\end{aligned} \quad (1)
$$

where ω_z is the Larmor frequency, d_{ij} the coupling constants, and $\hat{I}_x^i, \hat{I}_y^i, \hat{I}_z^i$ the spin operators that can be represented by $\hat{I}_u^i = \frac{1}{2}\hat{\sigma}_u$ with $\hat{\sigma}_u$ Pauli operators. $\widehat{\mathcal{H}}_z$ represents the Zeeman interaction and $\widehat{\mathcal{H}}_{dd}$ the dipolar interaction [53]. The latter is truncated to commute with the strong Zeeman interaction $(\omega_z \gg d_{ij})$, assuming that the effects of its noncommuting part are negligible. In a frame of reference rotating at the Larmor frequency [53], the Hamiltonian of the spin system reduces to $\widehat{\mathcal{H}}_{dd}$.

The quantum simulations start from the high-temperature thermal equilibrium [53]. Using the notation $\hat{I}_z = \sum_i \hat{I}_z^i$, we can write the thermal equilibrium state as

$$
\rho_0 \approx \left(\hat{1} + \frac{\hbar \omega_z}{k_B T} \hat{I}_z \right) \Big/ \mathrm{Tr}\{\hat{1}\}. \quad (2)
$$

The unity operator $\hat{1}$ commutes with all operators, including the Hamiltonian and the density operator. It does not contribute to the observable signal and it is therefore convenient to exclude it from the density operator. The resulting density operator for the initial state of the system is then $\hat{\rho}_0 \propto \hat{I}_z$. In this state, the spins are uncorrelated and the density operator commutes with the Hamiltonian $\widehat{\mathcal{H}}_{dd}$.

We performed all experiments on a home-built solid-state NMR spectrometer with a ^{1}H resonance frequency of $\omega_z/2\pi = 300$ MHz. The spins are the protons of polycrystalline adamantane, where the average strength of the average dipolar interaction, determined from the width of the resonance line, is 7.9 kHz.

III. GROWTH OF SPIN CLUSTERS

A. Cluster size

The spin clusters that we consider can be written in product operator form as

$$
\hat{I}_u^l \dots \hat{I}_v^o \hat{I}_w^p (u, v, w = x, y, z).
$$

Here, the indexes l, o, p identify the spins involved in the given cluster. We write K for the number of terms in this product, i.e., for the number of spins in the cluster. Experimentally, we generate these clusters using an NMR method developed by Pines and coworkers [54,55]. It is based on generating an average Hamiltonian $\widehat{\mathcal{H}}_0$ that does not commute with the thermal equilibrium state

$$
\begin{aligned}
\widehat{\mathcal{H}}_0 &= -\sum_{i<j} d_{ij} \left[\hat{I}_x^i \hat{I}_x^j - \hat{I}_y^i \hat{I}_y^j \right] \\
&= -\frac{1}{2} \sum_{i<j} d_{ij} [\hat{I}_+^i \hat{I}_+^j + \hat{I}_-^i \hat{I}_-^j], \quad (3)
\end{aligned}
$$

where $\hat{I}_\pm^j = (\hat{I}_x^j \pm i \hat{I}_y^j)$. In the usual computational basis, we write the states as $|M, n_M\rangle$ where M is the total magnetic quantum number, i.e., $\hat{I}_z|M, n_M\rangle = M|M, n_M\rangle$, and n_M distinguishes different states with the same M. The Hamiltonian (3) flips simultaneously two spins with the same orientation. Starting from the thermal equilibrium state, it generates a density operator where only elements ρ_{ij} with

$$
\Delta M = M(i) - M(j) = 2n, \quad n = 0, 1, 2, \dots
$$

are populated. The index i and j refer to the different spin states in the Zeeman basis as described above. Such a density operator element ρ_{ij} is called a ΔM quantum coherence. Off-diagonal elements with $\Delta M = 0$ represent zero quantum coherences, and diagonal elements correspond to populations.

Figure 1 shows a graphical representation of the density matrix in the computational basis. The black diagonal line represents the population elements of the density matrix. The diagonal blocks (gray) represent coherences of $\hat{\rho}$ with $\Delta M = 0$ and moving away from these diagonal blocks, the
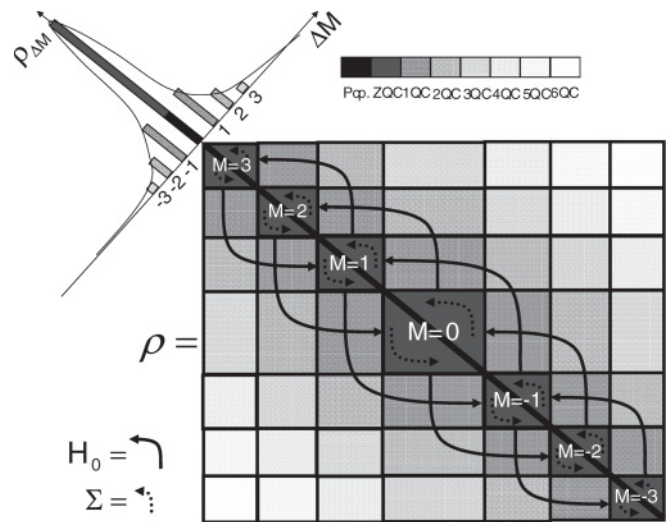

FIG. 1. Density matrix in the computational basis. The black diagonal line represents the populations (Pop. in the legend). The diagonal blocks (dark gray) represent coherences of $\hat{\rho}$ with $\Delta M = 0$ (ZQC) and the nondiagonal blocks are the ΔM multiple quantum coherence (MQC) blocks (gray tones). The solid and dashed arrows indicate the effect of $\widehat{\mathcal{H}}_0$ and the perturbation interaction $\Sigma = \widehat{\mathcal{H}}_{dd}$, respectively, on the thermal equilibrium density operator. A schematic representation of a typical distribution is given by the Gaussian-like shape in the top-left corner.

ΔM multiple quantum coherence (MQC) order increases, as represented by different gray values. The solid arrows indicate the effect of $\widehat{\mathcal{H}}_0$ on the thermal equilibrium density operator. Adding the elements of $\hat{\rho}$ with a given ΔM, we obtain a distribution function of the MQC elements of the density matrix $\hat{\rho}_{\Delta M}$. A schematic representation of its distribution is given by the Gaussian-like shape on the upper-left corner of Fig. 1. This distribution is initially a delta function on the diagonal of $\hat{\rho}$ and spreads with time.

To determine the average number of correlated spins, the technique relies on the fact that in a system of K spins, the number of transitions with a given ΔM follows a binomial distribution [56,57]

$$n(\Delta M, K) = \frac{(2K)!}{(K + \Delta M)!(K - \Delta M)!}. \quad (4)$$

For $K \gg 1$, the binomial distribution can be well approximated with a Gaussian

$$n(\Delta M, K) \propto \exp\left(-\frac{\Delta M^2}{K}\right), \quad (5)$$

whose half width at e^{-1} is $\sigma = \sqrt{K}$. Thus, we can determine the effective size of the spin clusters in a given state by measuring the distribution of the MQCs of its density operator ρ as a function of the coherence order ΔM.

B. Growth

Figure 2 shows two distribution functions of the MQCs for two different durations $N\tau_0$ of the evolution under $\widehat{\mathcal{H}}_0$. They clearly demonstrate the increasing width of the MQC distribution and thereby the increasing size of the spin clusters.
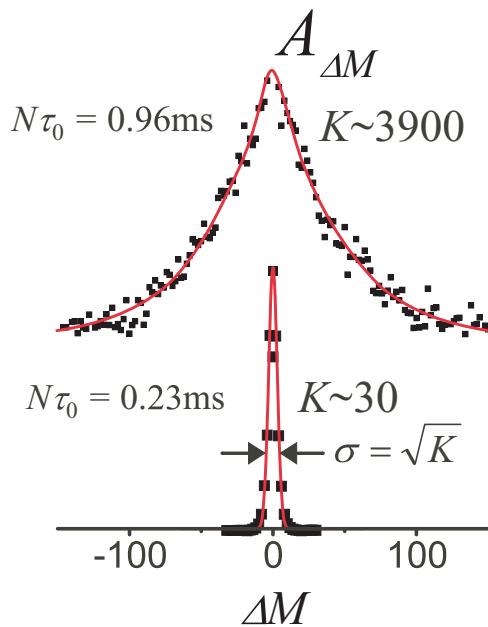

FIG. 2. (Color online) MQC distributions for two different evolution times. The cluster size is extracted from the variance $\sigma = \sqrt{K}$.

The elements of the density operator with a given ΔM can be distinguished by rotating the system around the z axis. A rotation $\hat{\phi}_z = e^{-i\phi \hat{I}_z}$ by ϕ changes the density operator as

$$\hat{\rho}(\phi, t) = \hat{\phi}_z \hat{\rho}(t) \hat{\phi}_z^\dagger = \sum_{\Delta M} \hat{\rho}_{\Delta M}(t) e^{i\Delta M \phi}, \quad (6)$$

where $\hat{\rho}(t) = e^{-i\widehat{\mathcal{H}}_0 t} \hat{\rho}_0 e^{i\widehat{\mathcal{H}}_0 t}$ and $\hat{\rho}_{\Delta M}(t)$ contains the elements that involve coherences of order ΔM. The experimental observables in NMR are $\hat{I}_x$, $\hat{I}_y$, and by means of a $\pi/2$ pulse, also $\hat{I}_z$. They are operators with $\Delta M = \pm 1$ or $\Delta M = 0$, respectively. Thus we are not able to measure all the elements of the density matrix. In order to quantify the $\hat{\rho}_{\Delta M}$ blocks, we use the pulse sequence shown in Fig. 3.

The system initially evolves for a period of duration $N\tau_0$ under the Hamiltonian $(\widehat{\mathcal{H}}_0)_\phi = \hat{\phi}_z \widehat{\mathcal{H}}_0 \hat{\phi}_z^\dagger$, i.e.,

$$
\begin{aligned}
\hat{\rho}_0 \xrightarrow{(\widehat{\mathcal{H}}_0)_\phi N\tau_0} \hat{\rho}_\phi(N\tau_0) &= \hat{\phi}_z \hat{\rho}(N\tau_0) \hat{\phi}_z^\dagger \\
&= \hat{\phi}_z e^{-i\widehat{\mathcal{H}}_0 N\tau_0} \hat{\rho}_0 e^{i\widehat{\mathcal{H}}_0 N\tau_0} \hat{\phi}_z^\dagger \\
&= \sum_{\Delta M} \hat{\phi}_z \hat{\rho}_{\Delta M}(N\tau_0) \hat{\phi}_z^\dagger \\
&= \sum_{\Delta M} \hat{\rho}_{\Delta M}(N\tau_0) e^{i\Delta M \phi}. \quad (7)
\end{aligned}
$$

A subsequent evolution period with the same duration $N\tau_0$ under $-\widehat{\mathcal{H}}_0$, which causes an evolution backward in time, yields the final density operator

$$
\begin{aligned}
\xrightarrow{(-\widehat{\mathcal{H}}_0)N\tau_0} \hat{\rho}_f(2N\tau_0) &= e^{i\widehat{\mathcal{H}}_0 N\tau_0} \hat{\rho}_\phi(N\tau_0) e^{-i\widehat{\mathcal{H}}_0 N\tau_0} \\
&= \sum_{\Delta M} \left[e^{i\widehat{\mathcal{H}}_0 N\tau_0} \hat{\rho}_{\Delta M}(N\tau_0) e^{-i\widehat{\mathcal{H}}_0 N\tau_0} \right] e^{i\Delta M \phi}.
\end{aligned}
$$
$$(8)$$

If $\hat{I}_z$ is the NMR observable, we obtain the signal

$$
\begin{aligned}
S(\phi, N\tau_0) &= \mathrm{Tr}\{\hat{I}_z \hat{\rho}_f(2N\tau_0)\} \\
&= \mathrm{Tr}\{e^{-i\widehat{\mathcal{H}}_0 N\tau_0} \hat{\rho}_0 e^{i\widehat{\mathcal{H}}_0 N\tau_0} \hat{\rho}_\phi(N\tau_0)\} \\
&= \mathrm{Tr}\{\hat{\rho}(N\tau_0) \hat{\rho}_\phi(N\tau_0)\} \\
&= \sum_{\Delta M} e^{i\phi \Delta M} \mathrm{Tr}\{\hat{\rho}_{\Delta M}^2(N\tau_0)\} \quad (9) \\
&= \sum_{\Delta M} e^{i\phi \Delta M} A(\Delta M), \quad (10)
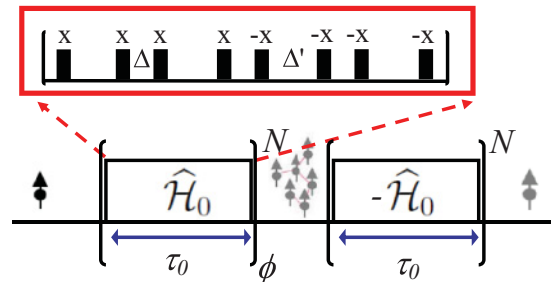\end{aligned}
$$

FIG. 3. (Color online) NMR sequence for generating large spin clusters. The effective Hamiltonian $\widehat{\mathcal{H}}_0$ is generated by the sequence of $\pi/2$ pulses shown in the upper part of the figure, where $\Delta' = 2\Delta + \tau_p$ and τ_p is the $\pi/2$ pulse duration [55].
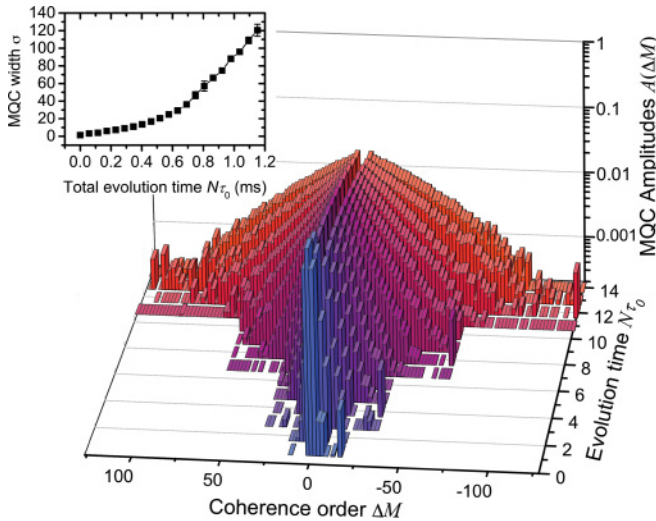
FIG. 4. (Color online) Time evolution of the MQC distribution. The main panel shows the time evolution of the MQC spectrum $A(\Delta M)$. The inset shows the time evolution of σ, where $A(\sigma, N\tau_0)/A(0, N\tau_0) = 1/e$.

where $A(\Delta M)$ are the amplitudes of the MQC spectrum. To extract these amplitudes from the experimental data, we measure the signal $S(\phi, N\tau_0)$ as a function of ϕ and perform a Fourier transform with respect to ϕ. We quantify the cluster size K by inverting the relation $A(\Delta M) = n(\Delta M, K)$ (see Ref. [55] for details).

If the system evolves under the Hamiltonian (3), the width of the $A(\Delta M)$ distribution increases indefinitely, as shown in Fig. 4. The main panel shows the MQC distributions $A(\Delta M)$ for different evolution times. We quantify the spreading of the MQC distribution by measuring their widths σ at $A(\sigma, N\tau_0)/A(0, N\tau_0) = 1/e$ for different evolution times. The inset of the figure shows the time evolution of σ. Equivalently, its corresponding cluster size of correlated spins also grows indefinitely, as shown in Fig. 5.
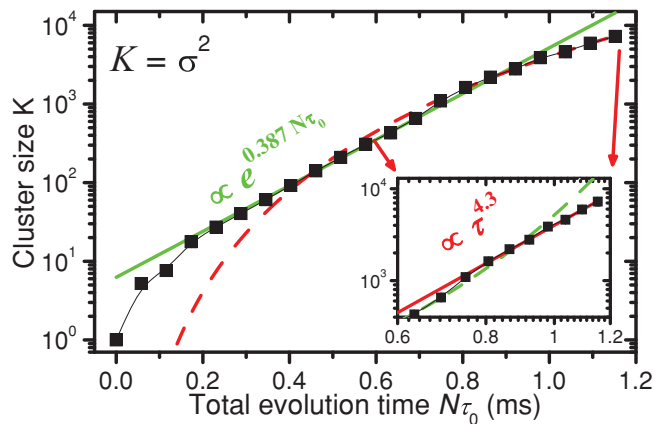

FIG. 5. (Color online) Time evolution of the cluster size of correlated spins with the Hamiltonian $\widehat{\mathcal{H}}_0$ (black square points). The main panel shows it in log scale manifesting the region where the growth is exponential, and the inset shows it in log-log scale manifesting its power law growth for long times.

The Hamiltonian of Eq. (3) is prepared by means of the standard NMR sequence [54,55] shown in the upper part of Fig. 3. This sequence consists of $\pi/2$ rotations of the spins separated by periods of free precession, Δ and Δ', under the dipolar Hamiltonian $\widehat{\mathcal{H}}_{dd}$ and it was shown to approximate quite well the ideal Hamiltonian $\widehat{\mathcal{H}}_0$. It is inverted experimentally by shifting the phase of all rf pulses by $\pm\pi/2$ [54]. We used pulse durations $\tau_{\pi/2} = 2.8$ μs and delays $\Delta = 2$ μs and $\Delta' = 2\Delta + \tau_p$ giving a cycle time $\tau_0 = 57.6$ μs.

C. MQC distributions and cluster size

In this section we summarize previous works that described the MQC distribution, its evolution, and how it is related to the cluster size of correlated spins in order to compare their results with our experimental observation. So far, it has not been possible to derive a consistent theoretical model of the processes involved in this type of many-body system. The most accepted and simplest model for interpreting the MQC distributions was proposed by Baum *et al.* [55]. It assumes equal excitation probabilities (for a given system size) for every coherence term of the density matrix and therefore predicts a Gaussian distribution whose variance is related to the number of correlated spins. This is the usually adopted model because it provides the simplest qualitative description of the MQC evolution. However, the experimentally observed distributions are not always Gaussian [58]. This is also the case in our experiments: the data shown in Fig. 4 are better described by an exponential distribution $A(\Delta M)$. Our results are therefore more consistent with the distribution discussed by Lacelle *et al.* [58], who predicted an exponential MQC distribution and found agreement with earlier experimental results from adamantane. Additionally, they predicted a dynamical scale invariance in the growth process of the MQC.

Due to the difficulty of treating many-spin systems rigorously, quantum-mechanical predictions for the MQC profile shapes and their interpretations are still missing. For example, if the MQC profile is not a Gaussian distribution, it is not trivial how to extract from it the cluster size. While most of the previous works studying the distribution of MQCs assumed Gaussian distributions, it is more convenient to use a parameter that is independent of the MQC distribution form. Khitrin proposed using the second moment of the MQC spectrum for this purpose [59]. This parameter was shown to be related to the second moment of the system Hamiltonian, in our case given by Eq. (3), and $K(t)$ is proportional to the second moment of the MQC distribution.

To determine the cluster size from our experimental data we measured the half width $\sigma = \sqrt{K}$ of the MQC distributions at $1/e$. We chose $\sigma = \sqrt{K}$ because an exponential MQC distribution of the form $\exp(-\Delta M/\sqrt{K(t)})$ has the same width as the Gaussian distribution (5). Assuming this distribution, its second moment is $2K$ while for a Gaussian distribution it is $K/2$. With the exception of the Gaussian model for a MQC distribution, there is no rigorous model that provides the exact factor that converts the second moment of the distribution to the cluster size K. However, they are of the same order of magnitude and thus the error of the cluster-size determination is a scale factor of order 1. In our experiments, the MQC

distribution has the same shape during the complete range of the experimentally accessible evolution time. Accordingly, any error of the determination of the cluster size is thus a constant factor independent of the value of K and this does not change the conclusions of this article.

The growth depends on the spin-coupling network topology as was observed experimentally [55,58–63]. Mainly three types of growth were observed: (i) indefinite growth, (ii) localized growth, and (iii) localized growth at a first stage (intramolecular-like localization) and then a further indefinite growth (intermolecular).

Results for adamantane fall into the first category. Some models suggest a power law for the growth [61,64] and these preliminary results [58,61] seem to match with an effective 3D spin-coupling network topology. That 3D behavior seems to be achieved only for cluster sizes above 1000 spins [61]. However, more recent works suggest an exponential growth of the cluster size when many neighboring spins are contained in the spin-coupling topology [62,63]. This is the case of adamantane and the experiments agree well with that prediction.

Experimentally, the data shown in Fig. 5 suggest three stages of the cluster size evolution: (i) An initial period where the evolution cannot be described as exponential or power law, (ii) a period of exponential growth, and (iii) a power law regime. During the first stage, the MQC distribution changes from a Gaussian-like distribution to an exponential distribution. Thus, the determination of the cluster size could be affected by two kinds of systematic errors: (i) at small cluster sizes, the small number of correlated spins may make the statistical assumptions questionable and (ii) the change of distribution from Gaussian to exponential may change the appropriate scale factors. The exponential growth agrees with the behavior expected by theoretical predictions for this kind of system [62,63]. And finally the power law behavior could be due to the following two reasons: (i) as predicted by Lacelle [61] after a certain number of spins (around 1000 in adamantane) the effective spin-network topology turns into a 3D spin-coupling network, which leads to a power law growth or (ii) because the experimental generation of $\widehat{\mathcal{H}}_0$ contains nonidealities, they can be considered as a perturbation that generates localization effects, as was demonstrated in Ref. [32] and discussed in the following sections. Something similar to the latter point could be interpreted from the predictions of Ref. [63].

IV. EFFECT OF PERTURBATION

A. Perturbed evolution

The evolution under the Hamiltonian $\widehat{\mathcal{H}}_0$ can be reversed completely by changing the Hamiltonian from $\widehat{\mathcal{H}}_0$ to $-\widehat{\mathcal{H}}_0$. If this time reversal is perfect, the signal (9) for phase $\phi = 0$ is independent of the evolution time $N\tau_0$, $\sum_{\Delta M} A(\Delta M, N\tau_0) =$ const.

Experimentally, the Hamiltonian $\widehat{\mathcal{H}}_0$ is generated as an effective Hamiltonian. Because of experimental imperfections, it always deviates from the ideal Hamiltonian (3). As a result, the actual dynamics deviates from the ideal one and, in particular, we cannot exactly invert the perturbed Hamiltonian and thus revert the time evolution. Because of the deviations in $\widehat{\mathcal{H}}_0$, the quantity $\sum_{\Delta M} A(\Delta M)$ is no longer conserved,

but decays with increasing evolution time. This decay is not uniform, but it affects mostly those components of the density operator that correspond to strongly delocalized coherence. As a result, the spreading of the information is attenuated and the system becomes effectively localized. It is this latter effect that we want to study here; we isolate it from the overall decrease of the signal by normalizing the MQC spectra such that the total signal $\sum_{\Delta M} A(\Delta M)$ for $\phi = 0$ is again constant in time.

To analyze this deviation from the ideal evolution, we introduce a perturbation $\widehat{\Sigma}$, whose strength we can control experimentally, and study the behavior of the system as a function of the perturbation strength. We choose the dipole-dipole coupling for this perturbation, $\widehat{\Sigma} = \widehat{\mathcal{H}}_{dd}$, which is a local interaction: every spin interacts mostly with its nearest neighbors, while the coupling strength with more distant spins drops off as $1/d^3$.

We add this Hamiltonian to the ideal Hamiltonian $\widehat{\mathcal{H}}_0$ by concatenating short evolution periods under $\widehat{\mathcal{H}}_{dd}$ with evolution periods under $\widehat{\mathcal{H}}_0$. We label the durations of the two time periods τ_Σ and τ_0, as shown in Fig. 6. When the duration $\tau_c = \tau_0 + \tau_\Sigma$ of each cycle is short compared to the inverse of the dipolar couplings d_{ij}, the resulting evolution can be described by the effective Hamiltonian

$$\widehat{\mathcal{H}}_{\text{eff}} = (1 - p)\widehat{\mathcal{H}}_0 + p\widehat{\Sigma}, \tag{11}$$

where the relative strength $p = \tau_\Sigma/\tau_c$ of the perturbation $\widehat{\Sigma} = \widehat{\mathcal{H}}_{dd}$ can be controlled by adjusting the duration τ_Σ. In the experiment, we compare the artificially perturbed evolution of $\widehat{\mathcal{H}}_{\text{eff}}$ with the $\widehat{\mathcal{H}}_0$ evolution with its intrinsic errors. While the intrinsic errors reduce the signal or the overall fidelity, they do not cause localization on the time scale of our experiments (see Fig. 5).

Considering now this perturbation, starting from thermal equilibrium, the state of the system at the end of N cycles is

$$\hat{\rho}^{\mathcal{H}_{\text{eff}}}(N\tau_c) = e^{-i\widehat{\mathcal{H}}_{\text{eff}}N\tau_c}\hat{\rho}_0\, e^{i\widehat{\mathcal{H}}_{\text{eff}}N\tau_c}. \tag{12}$$

Taking into account now the complete sequence of evolutions given by Fig. 6,

$$\hat{\rho}_0 \xrightarrow{(\widehat{\mathcal{H}}_{\text{eff}})_\phi N\tau_c} \hat{\rho}_\phi^{\mathcal{H}_{\text{eff}}}(N\tau_c) = \hat{\phi}_z\hat{\rho}^{\mathcal{H}_{\text{eff}}}(N\tau_c)\hat{\phi}_z^\dagger$$

$$= \hat{\phi}_z e^{-i\widehat{\mathcal{H}}_{\text{eff}}N\tau_c}\hat{\rho}_0 e^{i\widehat{\mathcal{H}}_{\text{eff}}N\tau_c}\hat{\phi}_z^\dagger$$

$$= \sum_{\Delta M}\hat{\phi}_z\hat{\rho}_{\Delta M}^{\mathcal{H}_{\text{eff}}}(N\tau_c)\hat{\phi}_z^\dagger$$

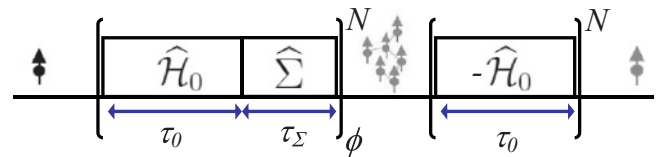$$= \sum_{\Delta M}\hat{\rho}_{\Delta M}^{\mathcal{H}_{\text{eff}}}(N\tau_c)e^{i\Delta M\phi}, \tag{13}$$

FIG. 6. (Color online) NMR sequence for the quantum simulations. A perturbed evolution is achieved when $\tau_\Sigma \neq 0$. The effective Hamiltonian $\widehat{\mathcal{H}}_0$ is generated by the sequence of $\pi/2$ pulses shown in the upper part of Fig. 3, and $\widehat{\Sigma} = \widehat{\mathcal{H}}_{dd}$ is the free evolution Hamiltonian.

$$\xrightarrow{(-\hat{\mathcal{H}}_0)N\tau_0} \hat{\rho}_f^{\mathcal{H}_{\text{eff}}}(N\tau_c + N\tau_0)$$

$$= e^{i\hat{\mathcal{H}}_0 N\tau_0}\hat{\rho}_\phi^{\mathcal{H}_{\text{eff}}}(N\tau_c)e^{-i\hat{\mathcal{H}}_0 N\tau_0}$$

$$= \sum_{\Delta M}\left[e^{i\hat{\mathcal{H}}_0 N\tau_0}\hat{\rho}_{\Delta M}^{\mathcal{H}_{\text{eff}}}(N\tau_c)e^{-i\hat{\mathcal{H}}_0 N\tau_0}\right]e^{i\Delta M\phi}. \quad (14)$$

Thus the NMR signal, which is measured after the last backward evolution $\exp\{i\hat{\mathcal{H}}_0 N\tau_0\}$, can be written as

$$S(\phi, N\tau_0 + N\tau_c) = \text{Tr}\left\{\hat{I}_z\hat{\rho}_f^{\mathcal{H}_{\text{eff}}}(N\tau_c + N\tau_0)\right\}$$

$$= \text{Tr}\left\{e^{-i\hat{\mathcal{H}}_0 N\tau_0}\hat{\rho}_0 e^{i\hat{\mathcal{H}}_0 N\tau_0}\hat{\rho}_\phi^{\mathcal{H}_{\text{eff}}}(N\tau_c)\right\}$$

$$= \text{Tr}\left\{\hat{\rho}^{\mathcal{H}_0}(N\tau_0)\hat{\rho}_\phi^{\mathcal{H}_{\text{eff}}}(N\tau_c)\right\}$$

$$= \sum_{\Delta M}e^{i\phi\Delta M}\text{Tr}\left\{\hat{\rho}_{\Delta M}^{\mathcal{H}_0}(N\tau_0)\hat{\rho}_{\Delta M}^{\mathcal{H}_{\text{eff}}}(N\tau_c)\right\} \quad (15)$$

$$= \sum_{\Delta M}e^{i\phi\Delta M}A(\Delta M). \quad (16)$$

Reinterpreting these expressions, we define the effective observable $\hat{\mathcal{A}} = e^{-i\hat{\mathcal{H}}_0 N\tau_0}\hat{\rho}_0 e^{i\hat{\mathcal{H}}_0 N\tau_0} = \hat{\rho}^{\mathcal{H}_0}(N\tau_0)$, where $\hat{\rho}^{\mathcal{H}_0}$ is the density operator of the unperturbed evolution. The NMR signal becomes then $S(\phi, N\tau_c) = \text{Tr}\{\hat{\mathcal{A}}\hat{\rho}_\phi^{\mathcal{H}_{\text{eff}}}(N\tau_c)\}$.

For the ideal evolution ($p = 0$), Eq. (9) is recovered, where $A(\Delta M)$ corresponds to the squared amplitudes of the density operator elements $\hat{\rho}_{\Delta M}^{\mathcal{H}_0}(N\tau_0)$ with coherence order ΔM. For the perturbed evolution ($p \neq 0$), they are reduced by the overlap of the actual density operator elements $\hat{\rho}_{\Delta M}^{\mathcal{H}_{\text{eff}}}(N\tau_c)$ with the ideal ones. We extract these amplitudes by performing a Fourier transformation with respect to ϕ. Figure 7 shows, as an example, the resulting $A(\Delta M)$ as a function of time for $p = 0.108$. The main panel represents the MQC distributions for different evolution times. The main difference compared to
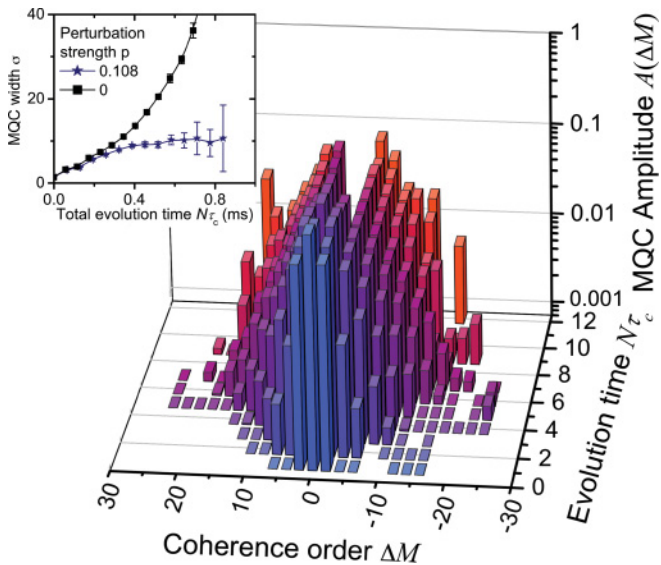

FIG. 7. (Color online) Time evolution of the MQC distribution under a perturbation $p = 0.108$. The main panel shows the time evolution of the MQC spectrum $A(\Delta M)$. The inset shows the time evolution of the standard deviation σ for the unperturbed case compared with the perturbed case. This comparison shows directly the localization.
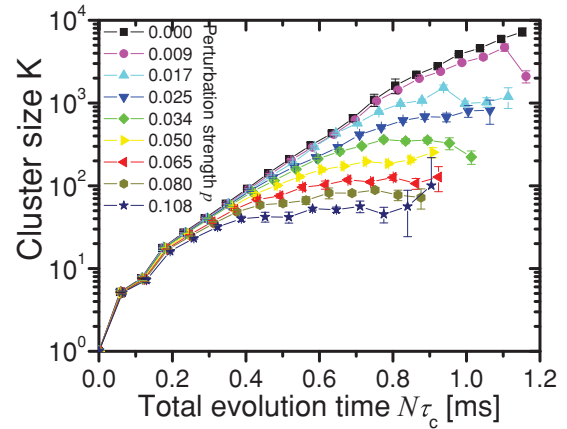

FIG. 8. (Color online) Time evolution of the cluster size for different perturbation strengths. The black squares represent the unperturbed time evolution and the other symbols correspond to the perturbed evolutions according to the legend.

Fig. 4 is that the MQC spectrum does not spread indefinitely [32]. We consider this saturation of the spreading of the MQC spectrum evolution as evidence of localization due to the perturbation (see below). The localization effects are easily visualized by directly comparing the generation of high-order multiple quantum coherences of the unperturbed case of Fig. 4 with the perturbed one of Fig. 7. While the distribution spreads continuously in Fig. 4, it reaches a limiting value in Fig. 7. The inset of Fig. 7 shows the time evolution of the width σ for $p = 0.108$ compared with the unperturbed case.

From the width of the MQC spectrum, we calculate the size of the spin clusters. The black squares of Fig. 8 show the average number of correlated spins as a function of time for an unperturbed evolution, $p = 0$. This is the log scale representation of the curve of Fig. 5. The other symbols of the figure show the evolution of the number of correlated spins for different values of p. Initially, the cluster size $K(N\tau_c)$ starts to grow as in the unperturbed evolution, but then it saturates after a time that decreases with increasing perturbation strength p. As we explained above, we consider this as evidence of localization induced by the perturbation and it is related to spatial localization. The size of the cluster at which this saturation occurs is also determined by the strength of the perturbation: increasing perturbation strength reduces the limiting cluster size.

B. Interpretation

The terms in Eq. (15) are related to the fidelity of the corresponding density operator component $\hat{\rho}_{\Delta M}$ with respect to the corresponding component resulting from the unperturbed evolution

$$f_{\Delta M} = \frac{\text{Tr}\left\{\hat{\rho}_{\Delta M}^{\mathcal{H}_0}(N\tau_0)\hat{\rho}_{\Delta M}^{\mathcal{H}_{\text{eff}}}(N\tau_c)\right\}}{\text{Tr}\left\{\hat{\rho}_{\Delta M}^{\mathcal{H}_0}(N\tau_0)\hat{\rho}_{\Delta M}^{\mathcal{H}_0}(N\tau_0)\right\}}, \quad (17)$$

which reaches unity for vanishing perturbation ($p = 0$). We therefore consider the reduction as a quantitative measure of the effect of the perturbation. The decoherence of different ΔM blocks of the density matrix was studied when a given quantum state prepared by evolution under $\hat{\mathcal{H}}_0$ evolves under

a pure $\widehat{\mathcal{H}}_{dd} = \widehat{\Sigma}$ perturbation [9,13]. However, the quantification and characterization of how a perturbation disturbs the different blocks of the density matrix during the creation of spin-cluster states is still not known. This merits further studies like that in Ref. [65]. Here, we focus only on the effect on the number of correlated spins and do not consider the change of the overall amplitude. Thus we normalize the integral of each spectrum and determine its width by fitting it to a Gaussian or an exponential.

The spreading of the MQC spectrum is generated by the effective Hamiltonian created with the sequence of Fig. 1. The cluster size that we determine here corresponds to an overlap of the actual state with the ideal state resulting from unperturbed evolution. This is similar to the fidelity measure in quantum computing, where the agreement between the actual state of the system with the target state is measured. In our case, the target state is a growing cluster, while the actual state grows only for some time until it reaches a limiting size, which is typical for localization. The size of this localized state decreases with increasing perturbation strength.

During our experiment, the magnetization is uniform throughout the sample, so the process does not lead to a spatial redistribution of magnetization. However, since we measure the number of correlated spins, we can attribute a length scale to the resulting state. Given a suitable initial state, the same process would generate highly entangled multiqubit states. In the presence of a perturbation, the number of qubits that can be entangled in this way is limited to the size of the resulting cluster.

V. EVIDENCE FOR A DYNAMICAL EQUILIBRIUM CLUSTER SIZE

The experimental results presented above show that the cluster size reaches a stationary value. It remains to be seen if this limiting size results from a slowdown in the growth [29] or if it represents a dynamic equilibrium state. We showed that actually the cluster size achieves a dynamical equilibrium state [32]. In order to do that, we repeated the previous experiment for a series of initial conditions corresponding to different clusters sizes. Figure 9 shows the corresponding pulse sequence: the initial state preparation, consisting of an evolution of duration $N_0\tau_0$ under the unperturbed Hamiltonian $\widehat{\mathcal{H}}_0$, generates clusters of size K_0. During the subsequent
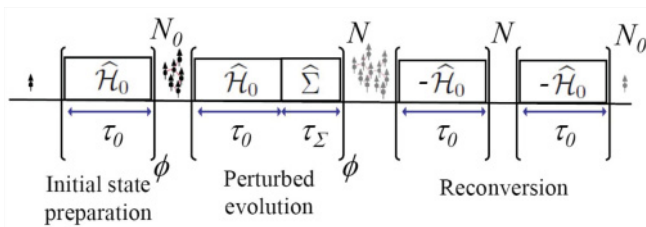

FIG. 9. (Color online) NMR pulse sequence for preparing different initial clusters sizes and subsequently evolving them in the presence of a perturbation.
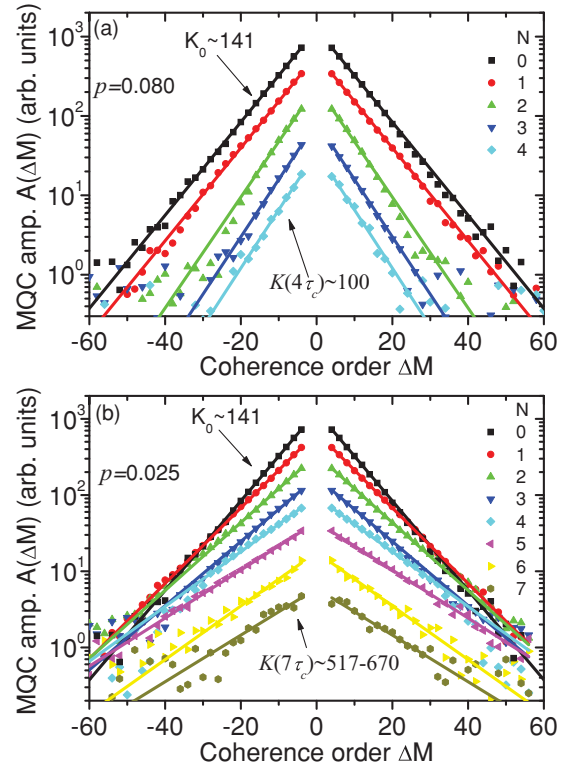

FIG. 10. (Color online) Time evolution of the MQC distribution in the presence of a perturbation starting from an initial sate with $K_0 \simeq 141$ correlated spins. The initial MQC distribution of the initial state is given by the black squares and other colored symbols give its further time evolution for two different perturbation strengths: (a) $p = 0.080$ and (b) $p = 0.025$.

perturbed evolution of duration $N\tau_\mathrm{c}$, these initial clusters evolve and Eq. (15) becomes

$$S(\phi, N\tau_\mathrm{c}) = \sum_{\Delta M} e^{i\phi\Delta M} A(\Delta M)$$
$$= \sum_{\Delta M} e^{i\phi\Delta M} \mathrm{Tr}\left\{\hat{\rho}^{\mathcal{H}_0}_{\Delta M}(N\tau_0, N_0\tau_0)\hat{\rho}^{\mathcal{H}_\mathrm{eff}}_{\Delta M}(N\tau_c, N_0\tau_0)\right\}.$$
$$(18)$$

Figure 10 shows the results from these measurements. The symbols represent the amplitudes $A(\Delta M)$ of the different multiple quantum coherences as a function of the coherence order ΔM for different evolution times. The time evolution starts from an initial cluster size $K_0 = 141$ for two different perturbations strengths: $p = 0.080$ and $p = 0.025$. In this figure, the $A(\Delta M)$ values are not normalized. We find that the width of the MQC distributions contracts as a function of time in Fig. 10(a), but expands in Fig. 10(b). As in the case where we start from size $K_0 = 1$, this expansion does not continue indefinitely, but it saturates. Similarly, the contraction also reaches an equilibrium value. This is evident at the longest evolution times, where the gradients of the MQC distributions, which give the cluster sizes, are parallel in the semi-log-scale representation.

To quantify this, we determined the width of the MQC spectra and from that the cluster size. Figure 11 shows the evolution of the cluster size when we start from the
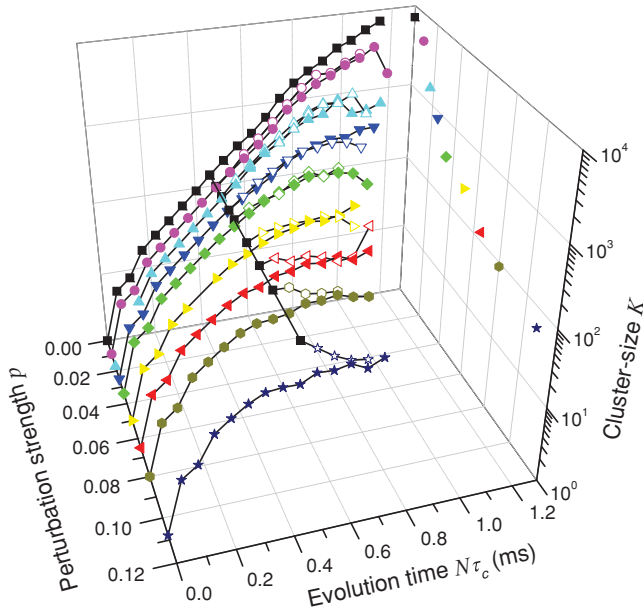
FIG. 11. (Color online) Time evolution of the cluster size starting from two different initial states as a function of the perturbation strength. Filled symbols are evolutions from an uncorrelated initial state ($K_0 = 1$) and the empty symbols start from an initial state with $K_0 = 141$ correlated spins (marked with black squares joined with a solid line). The equilibrium cluster sizes are represented by symbols in the K-p plane.

initial value $K_0 = 141$ for different perturbation strengths (empty symbols). The solid symbols represent the cluster-size evolution starting from $K_0 = 1$, i.e., the curves shown in Fig. 8. For all perturbation strengths, the time series for a given perturbation strength converges to the same limiting value, independent of the initial condition. Thus, we find that the evolution leads to a limiting cluster size that varies with the perturbation strength p, but does not depend on the initial condition K_0. The limiting cluster sizes are represented by the symbols on the K-p plane in Fig. 11.

This is again confirmed by the results shown in Fig. 12, which summarizes the results for additional initial values and two perturbation strengths, $p = 0.034$ and $p = 0.065$. The filled symbols correspond to uncorrelated initial states ($K_0 = 1$) and the empty symbols to various initial cluster sizes. For a given perturbation strength, the size of the spin clusters tends toward the same limiting value, independent of the initial condition.

VI. LOCALIZATION SIZE VS PERTURBATION STRENGTH

A. Experimental evidence

According to Figs. 8, 11, and 12, the size of the dynamical equilibrium clusters decreases with increasing strength of the perturbation. For a quantitative analysis of this dependence, we determined the size of the localized clusters from the data shown in Figs. 8, 11, and 12 and plotted them against the perturbation strength in Fig. 13. The yellow or light gray diagonal band in the figure represents a linear fit to the experimental data that gives $K_{\mathrm{loc}} \sim p^{-1.86 \pm 0.05}$, i.e., the

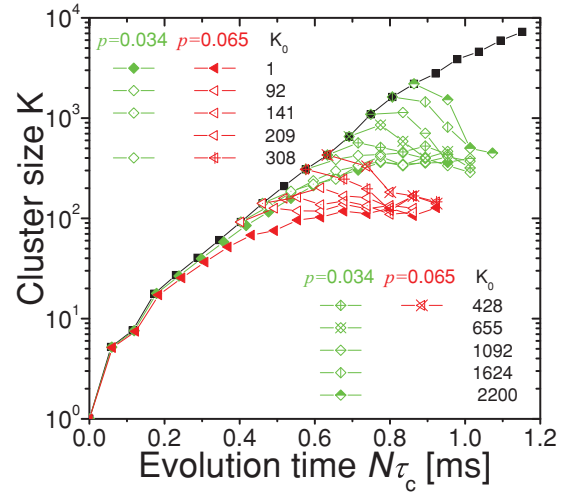FIG. 12. (Color online) Time evolution of the cluster size starting from different initial sates. Filled symbols are evolutions from an uncorrelated initial state for two different perturbation strengths given in the legend. Empty symbols start from an initial state with K_0 correlated spins.

cluster size decreases almost proportionally to the square of the perturbation strength. The error of the fit is indicated by the width of the band. The limiting value for $p = 1$, $K_{\mathrm{loc}} \approx 1$, is consistent with the expectation that the system becomes completely localized if the perturbation strength is significantly larger than the unperturbed Hamiltonian.

The figure also summarizes the evolution of the cluster size before the static (localized) size is reached. If the initial size is larger than the stationary value for the given perturbation strength, $K_0 > K_{\mathrm{loc}}$, the cluster shrinks [inset (a) in Fig. 13, above the diagonal]. If it is smaller, $K_0 < K_{\mathrm{loc}}$, the size increases with time [inset (b), below the diagonal].
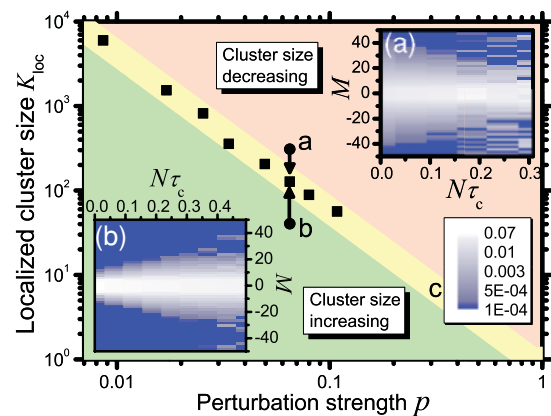

FIG. 13. (Color online) Localized cluster size K_{loc} (square symbols) of correlated spins vs the perturbation strength p. Three dynamical regimes for the evolution of the cluster size are identified depending on the number of correlated spins compared with the perturbation-dependent localization value: (a) cluster size decreases, (b) cluster size increases, and (c) stationary regime.

B. Phenomenological model

A theoretical model that describes this behavior would be highly desirable but is beyond the scope of this paper. Instead, we describe here a simple phenomenological model that summarizes the observed behavior. For this purpose, we write the amplitudes of the MQC spectra as

$$A(\Delta M, t) = A e^{-\Delta M / \sqrt{K(t)}}. \tag{19}$$

The exponential form agrees with the experimental data (see, e.g., Figs. 4 and 10). According to Fig. 5, the growth of the cluster size is exponential during a large part of the experiment. It may then be described by a differential equation of the type

$$\frac{dK}{dt} = \alpha K, \tag{20}$$

where α is the growth rate, which is proportional to the second moment of the NMR resonance line [62].

To derive an equation of motion for the perturbed evolution, we first consider the effect of the perturbation alone. As we have shown before [9], the interaction with the environment causes a decay of the MQC amplitudes that depends on the MQC order ΔM. It was shown in Ref. [9] that over the range of our measurements the decay rate is almost $\propto \Delta M$. The decay of the MQC amplitudes during a time τ is thus $\delta A(\Delta M) \propto -A(\Delta M) \Delta M p b \tau$, where p is the perturbation strength introduced above and b is the decay rate of single quantum coherences under the full perturbation, $p = 1$.

During a short time τ, the MQC spectrum evolves thus from Eq. (19) to

$$A(\Delta M, t + \tau) = A e^{-\Delta M (1/\sqrt{K_1(t+\tau)} + p b \tau)}.$$

Here, $K_1 = K_0(1 + \alpha \tau)$ is the size that the cluster size would reach, starting from K_0 in the absence of the perturbation. We can rewrite this as

$$A(\Delta M, t + \tau) = A e^{-\Delta M / \sqrt{K_1'(t+\tau)}},$$

with

$$
\begin{aligned}
K_1' &= \frac{K_0(1 + \alpha \tau)}{[1 + \sqrt{K_0(1 + \alpha \tau)} p b \tau]^2} \\
&= \frac{K_0(1 + \alpha \tau)}{1 + 2\sqrt{K_0(1 + \alpha \tau)} p b \tau + K_0(1 + \alpha \tau)(p b \tau)^2},
\end{aligned} \tag{21}
$$

where for short τ,

$$
\begin{aligned}
K_1' &\approx \frac{K_0(1 + \alpha \tau)}{1 + 2\sqrt{K_0(1 + \alpha \tau)} p b \tau} \\
&\approx K_0(1 + \alpha \tau)[1 - 2\sqrt{K_0(1 + \alpha \tau)} p b \tau].
\end{aligned} \tag{22}
$$

We now look for the stationary solution where $K_1' = K_0$:

$$K_1' = K_0 = K_0(1 + \alpha \tau)[1 - 2\sqrt{K_0(1 + \alpha \tau)} p b \tau]. \tag{23}$$

If we consider only terms of $O(\tau)$ in the infinitesimal time τ, this is equivalent to

$$(\alpha - 2\sqrt{K_0} p b) = 0. \tag{24}$$

Solving for K_0, we find the stationary cluster size as

$$K_{\text{loc}} = \left(\frac{\alpha}{2bp} \right)^2. \tag{25}$$

Considering the simplicity of this phenomenological model, this result agrees reasonably well with the experimentally observed behavior.

VII. DISCUSSION AND CONCLUSIONS

As a step toward improved understanding of the evolution of large quantum systems, we have studied the spreading of information in a system of nuclear spins. Starting with single qubits, the information can spread to clusters of several thousand qubits. While decoherence is well known to limit the time for which quantum information can be used, we focused here on its effect on the distance over which a quantum state can be transferred. For that purpose, a locally stored state was left to evolve in a 3D spin-coupling network. Using standard NMR techniques, we generated a Hamiltonian $\widehat{\mathcal{H}}_0$ that spreads the information and allows one to quantify the size of the resulting cluster of correlated spins. By comparing this unperturbed evolution with the evolution where a perturbation Hamiltonian of variable strength is added to $\widehat{\mathcal{H}}_0$, we showed that the information becomes localized on a distance scale that decreases with increasing perturbation strength.

Our experimental results demonstrate that a common dynamic equilibrium size of the localized state is achieved independent of the initial state consisting of different numbers of correlated spins. We developed a phenomenological model to describe these effects, which may be attributed to the competition between the spreading evolution driven by $\widehat{\mathcal{H}}_0$ and its systematic reduction due to decoherence induced by the perturbation. These results are related to theoretical predictions on similar systems that indicate a slowdown of the spreading [29] and can induce localized states with a finite cluster size [66]. Further extensions of these previous works could show if a dynamical equilibrium independent of the initial state appears as in our experiments. These previous works have considered disorder as the perturbation that produces Anderson localization.

The results presented here show a transition in the spin dynamics from an indefinite spreading to a localized dynamics. A spin far away from the spin where the initial condition is stored would receive excitation at some time if the perturbation is below a critical value; however, if the perturbation exceeds this threshold, no excitation will arrive at this site. Our experiments show a transition for the cluster-size dynamics: if the cluster size of the initial state exceeds the localization value, then it shrinks until it reaches the equilibrium value, but when the initial cluster size is lower than the localization value, it grows.

These results may also be connected to our earlier findings that the decoherence rate of quantum states with many correlated qubits increases with the size of the system [9] as $\sqrt{K}$, indicating that larger systems are more sensitive to perturbations. This increasing of the decoherence rate as the system size increases balances the tendency of the system to spread.

[1] T. D. Ladd, F. Jelezko, R. Laflamme, Y. Nakamura, C. Monroe, and J. L. O'Brien, Nature (London) **464**, 45 (2010).

[2] P. W. Shor, in *Proceedings of the 35th Annual Symposium on the Foundations of Computer Science*, edited by S. Goldwasser (IEEE Computer Society Press, Los Alamitos, CA, 1994), p. 124.

[3] D. P. DiVincenzo, Science **270**, 255 (1995).

[4] M. A. Nielsen and I. L. Chuang, *Quantum Computation and Quantum Information* (Cambridge University, Cambridge, England, 2000).

[5] H. D. Raedt and K. Michielsen, in *Handbook of Theoretical and Computational Nanotechnology. Quantum and Molecular Computing, Quantum Simulations*, edited by M. Rieth and W. Schommers (American Scientific, Valencia, CA, 2006).

[6] W. Zhang, N. Konstantinidis, K. A. Al Hassanieh, and V. V. Dobrovitski, J. Phys. Condens. Matter **19**, 083202 (2007).

[7] S. Popescu, A. J. Short, and A. Winter, Nature Phys. **2**, 754 (2006).

[8] G. A. Álvarez, E. P. Danieli, P. R. Levstein, and H. M. Pastawski, Phys. Rev. Lett. **101**, 120503 (2008).

[9] H. G. Krojanski and D. Suter, Phys. Rev. Lett. **93**, 090501 (2004).

[10] H. G. Krojanski and D. Suter, Phys. Rev. Lett. **97**, 150503 (2006).

[11] M. Lovric, H. G. Krojanski, and D. Suter, Phys. Rev. A **75**, 042305 (2007).

[12] W. H. Zurek, Rev. Mod. Phys. **75**, 715 (2003).

[13] H. G. Krojanski and D. Suter, Phys. Rev. A **74**, 062319 (2006).

[14] H. J. Cho, P. Cappellaro, D. G. Cory, and C. Ramanathan, Phys. Rev. B **74**, 224434 (2006).

[15] C. M. Sánchez, H. M. Pastawski, and P. R. Levstein, Physica B **398**, 472 (2007).

[16] H. M. Pastawski, P. R. Levstein, G. Usaj, J. Raya, and J. A. Hirschinger, Physica A **283**, 166 (2000).

[17] R. A. Jalabert and H. M. Pastawski, Phys. Rev. Lett. **86**, 2490 (2001).

[18] L. Viola, E. Knill, and S. Lloyd, Phys. Rev. Lett. **82**, 2417 (1999).

[19] D. A. Lidar, I. L. Chuang, and K. B. Whaley, Phys. Rev. Lett. **81**, 2594 (1998).

[20] J. Preskill, Proc. R. Soc. London A **454**, 385 (1998).

[21] E. Knill, Nature (London) **434**, 39 (2005).

[22] E. M. Fortunato, L. Viola, M. A. Pravia, E. Knill, R. Laflamme, T. F. Havel, and D. G. Cory, Phys. Rev. A **67**, 062303 (2003).

[23] T. Monz *et al.*, Phys. Rev. Lett. **103**, 200503 (2009).

[24] M. J. Biercuk, H. Uys, A. P. VanDevender, N. Shiga, W. M. Itano, and J. J. Bollinger, Nature (London) **458**, 996 (2009).

[25] J. Du, X. Rong, N. Zhao, Y. Wang, J. Yang, and R. B. Liu, Nature (London) **461**, 1265 (2009).

[26] A. A. Pomeransky and D. L. Shepelyansky, Phys. Rev. A **69**, 014302 (2004).

[27] G. DeChiara, D. Rossini, S. Montangero, and R. Fazio, Phys. Rev. A **72**, 012323 (2005).

[28] J. P. Keating, N. Linden, J. C. F. Matthews, and A. Winter, Phys. Rev. A **76**, 012315 (2007).

[29] C. K. Burrell and T. J. Osborne, Phys. Rev. Lett. **99**, 167201 (2007).

[30] T. Apollaro and F. Plastina, Open Syst. Inform. Dyn. **14**, 41 (2007).

[31] J. Allcock and N. Linden, Phys. Rev. Lett. **102**, 110501 (2009).

[32] G. A. Álvarez and D. Suter, Phys. Rev. Lett. **104**, 230403 (2010).

[33] G. A. Álvarez, E. P. Danieli, P. R. Levstein, and H. M. Pastawski, Phys. Rev. A **82**, 012310 (2010).

[34] A. Zwick and O. Osenda, J. Phys. A **44**, 105302 (2011).

[35] S. Bose, Phys. Rev. Lett. **91**, 207901 (2003).

[36] M. Christandl, N. Datta, A. Ekert, and A. J. Landahl, Phys. Rev. Lett. **92**, 187902 (2004).

[37] Z. L. Mádi, B. Brutscher, T. Schulte-Herbrüggen, R. Brüschweiler, and R. R. Ernst, Chem. Phys. Lett. **268**, 300 (1997).

[38] M. A. Nielsen, E. Knill, and R. Laflamme, Nature (London) **396**, 52 (1998).

[39] J. Zhang, G. L. Long, W. Zhang, Z. Deng, W. Liu, and Z. Lu, Phys. Rev. A **72**, 012331 (2005).

[40] J. Zhang, N. Rajendran, X. Peng, and D. Suter, Phys. Rev. A **76**, 012317 (2007).

[41] G. A. Álvarez, M. Mishkovsky, E. P. Danieli, P. R. Levstein, H. M. Pastawski, and L. Frydman, Phys. Rev. A **81**, 060302(R) (2010).

[42] P. Cappellaro, C. Ramanathan, and D. G. Cory, Phys. Rev. A **76**, 032317 (2007).

[43] E. Rufeil-Fiori, C. M. Sanchez, F. Y. Oliva, H. M. Pastawski, and P. R. Levstein, Phys. Rev. A **79**, 032324 (2009).

[44] W. Zhang, P. Cappellaro, N. Antler, B. Pepper, D. G. Cory, V. V. Dobrovitski, C. Ramanathan, and L. Viola, Phys. Rev. A **80**, 052323 (2009).

[45] G. A. Álvarez, E. P. Danieli, P. R. Levstein, and H. M. Pastawski, J. Chem. Phys. **124**, 194507 (2006).

[46] E. P. Danieli, G. A. Álvarez, P. R. Levstein, and H. M. Pastawski, Solid State Commun. **141**, 422 (2007).

[47] I. Rotter, J. Phys. A **42**, 153001 (2009).

[48] I. Rotter, J. Opt. **12**, 065701 (2010).

[49] I. Rotter, e-print arXiv:1011.0645.

[50] G. A. Álvarez, P. R. Levstein, and H. M. Pastawski, Physica B **398**, 438 (2007).

[51] P. W. Anderson, Phys. Rev. **109**, 1492 (1958).

[52] P. W. Anderson, Rev. Mod. Phys. **50**, 191 (1978).

[53] C. P. Slichter, *Principles of Magnetic Resonance*, 2nd ed. (Springer-Verlag, Berlin,1992).

[54] W. S. Warren, S. Sinton, D. P. Weitekamp, and A. Pines, Phys. Rev. Lett. **43**, 1791 (1979).

[55] J. Baum, M. Munowitz, A. N. Garroway, and A. Pines, J. Chem. Phys. **83**, 2015 (1985).

[56] A. Wokaun and R. R. Ernst, Mol. Phys. **36**, 317 (1978).

[57] R. A. Hoffman, Adv. Magn. Opt. Reson. **4**, 87 (1970).

[58] S. Lacelle, S. Hwang, and B. C. Gerstein, J. Chem. Phys. **99**, 8407 (1993).

[59] A. K. Khitrin, Chem. Phys. Lett. **274**, 217 (1997).

[60] J. Baum and A. Pines, J. Am. Chem. Soc. **108**, 7447 (1986).

[61] S. Lacelle, Adv. Magn. Opt. Reson. **16**, 173 (1991).

[62] V. Zobov and A. Lundin, JETP **103**, 904 (2006).

[63] V. E. Zobov and A. A. Lundin, Russ. J. Phys. Chem. B **2**, 676 (2008).

[64] K. K. Gleason, Concepts Magn. Reson. **5**, 199 (1993).

[65] S. I. Doronin, E. B. Fel'dman, and A. I. Zenchuk, J. Chem. Phys. **134**, 034102 (2011).

[66] M. Znidaric, T. Prosen, and P. Prelovsek, Phys. Rev. B **77**, 064426 (2008).